

## Connected pathway relative permeability from pore-scale imaging of imbibition



S. Berg<sup>a,\*</sup>, M. Rücker<sup>a,b</sup>, H. Ott<sup>c,a</sup>, A. Georgiadis<sup>a</sup>, H. van der Linde<sup>a</sup>, F. Enzmann<sup>b</sup>, M. Kersten<sup>b</sup>, R.T. Armstrong<sup>d</sup>, S. de With<sup>e</sup>, J. Becker<sup>f</sup>, A. Wiegmann<sup>f</sup>

<sup>a</sup> Shell Global Solutions International B.V., Kessler Park 1, 2288 GS Rijswijk, The Netherlands

<sup>b</sup> Geosciences Institute, Johannes Gutenberg University, Becherweg 21, 55099 Mainz, Germany

<sup>c</sup> Department of Petroleum Engineering, Montanuniversität Leoben, A-8700 Leoben, Austria

<sup>d</sup> School of Petroleum Engineering, University of New South Wales, NSW 2052 Sydney, Australia

<sup>e</sup> Technical University of Delft, The Netherlands

<sup>f</sup> Math2Market GmbH, Stiftsplatz 5, 67655 Kaiserslautern, Germany

### ARTICLE INFO

#### Article history:

Received 25 June 2015

Revised 25 January 2016

Accepted 30 January 2016

Available online 11 February 2016

#### Keywords:

X-ray tomography

Pore scale

Relative permeability

Multiphase flow

Drainage

Imbibition

### ABSTRACT

Pore-scale images obtained from a synchrotron-based X-ray computed micro-tomography ( $\mu$ CT) imbibition experiment in sandstone rock were used to conduct Navier–Stokes flow simulations on the connected pathways of water and oil phases. The resulting relative permeability was compared with steady-state Darcy-scale imbibition experiments on 5 cm large twin samples from the same outcrop sandstone material. While the relative permeability curves display a large degree of similarity, the endpoint saturations for the  $\mu$ CT data are 10% in saturation units higher than the experimental data. However, the two datasets match well when normalizing to the mobile saturation range. The agreement is particularly good at low water saturations, where the oil is predominantly connected. Apart from different saturation endpoints, in this particular experiment where connected pathway flow dominates, the discrepancies between pore-scale connected pathway flow simulations and Darcy-scale steady-state data are minor overall and have very little impact on fractional flow. The results also indicate that if the pore-scale fluid distributions are available and the amount of disconnected non-wetting phase is low, quasi-static flow simulations may be sufficient to compute relative permeability. When pore-scale fluid distributions are not available, fluid distributions can be obtained from a morphological approach, which approximates capillary-dominated displacement. The relative permeability obtained from the morphological approach compare well to drainage steady state whereas major discrepancies to the imbibition steady-state experimental data are observed. The morphological approach does not represent the imbibition process very well and experimental data for the spatial arrangement of the phases are required. Presumably for modeling imbibition relative permeability an approach is needed that captures moving liquid–liquid interfaces, which requires viscous and capillary forces simultaneously.

© 2016 The Authors. Published by Elsevier Ltd.

This is an open access article under the CC BY license (<http://creativecommons.org/licenses/by/4.0/>).

### 1. Introduction

For the description of multiphase flow in porous media on the Darcy scale, commonly the (phenomenological) extension of Darcy's law to multiphase is employed. The concept of relative permeability is introduced [21,26] to account for the presence of other immiscible fluid phases [61]. Together with the standard parameters porosity  $\phi$ , (absolute) permeability  $K$ , fluid viscosities  $\mu_i$ , and the capillary pressure  $p_c$  vs saturation  $S_w$  function, the relative

permeability  $k_r$  is one of the key parameters to model the flow of multiple phases. For instance, in reservoir engineering, where on the field scale viscous forces dominate over capillary forces [36], the relative permeability vs. saturation function together with absolute permeability has a large influence on the flux of fluid phases. Relative permeability can largely vary depending on rock type, wettability and other parameters, which can have a major impact on oil recovery by water flooding. At the same time, relative permeability is difficult and is experimentally time-consuming to obtain.

Since the multiphase extension of Darcy's law is phenomenological it does not within its own boundaries predict relative permeability. Relative permeability is traditionally determined

\* Corresponding author. Tel.: +31 704476161.

E-mail address: [steffen.berg@shell.com](mailto:steffen.berg@shell.com) (S. Berg).

experimentally using either the steady state [22,47] or non-steady state methods [11,46], which are time-consuming and costly. Therefore within the last decade there has been increasing interest in predicting relative permeability by pore-scale simulation [15], e.g. using pore network modeling or direct simulation techniques [27,31,48,51]. Generally these approaches can be categorized into pore network models [30,52,68] and direct approaches depending on whether the modeling is performed on a network model abstracted from the pore space or directly on the pore space obtained from X-ray computed micro-tomography ( $\mu$ CT) [28,50,51,55,62,63,79].

Pore-scale modeling approaches can be further categorized into quasi-static and dynamic approaches where capillary and viscous forces act at the same time [54]. Combinations of all categories exist, i.e. there are quasi-static [15] and dynamic pore network models ([30,32,45]), but also quasi-static [8] and dynamic direct simulation methods [14,16,17,20,24,27,31,43,65–67,78]. In practice, the most common approaches are quasi-static pore network models, which are computationally less costly than dynamic and direct approaches due to simplifications made. However, these simplifications introduce uncertainty. First, the abstracted pore networks are often subject to tuning on reference data (e.g. capillary-pressure data), which decreases a direct link between the actual pore space and the abstracted network [64]. Elementary pore-scale displacement events [52] are captured only in a mechanistic way. Then the capillary-viscous flow is decomposed into capillary-dominated steps determining the pore-scale saturation distribution and viscous-dominated steps where the hydraulic conductivity of connected phases are determined. The main limitation of quasi-static pore network modeling is that only the connected pathway flow is captured. However, multiphase flow in porous media consists of connected flow and ganglion dynamics [57,81] caused by the motion of disconnected fluid phases [23,72,80]. In reality there is mass exchange between connected and disconnected fluid phases [33–35], which not only adds to the net flux but also influences the time evolution of the pore-scale fluid distributions, including the configuration of connected phases.

Dynamic pore network models are more sophisticated and attempt to capture dynamics effects like capillary-viscous displacement including ganglion dynamics correctly [32,45], but are more expensive from a computational perspective. Direct dynamic simulation approaches based on the lattice Boltzmann technique [17,19,20,24,67] and Navier–Stokes approaches ([27,31,43,65,66]) are becoming more popular because no a priori choice between level of rigor and captured phenomena are made. Like other dynamic approaches, capillary and viscous forces act at the same time and, depending on the choice of flow parameters, both capillary and viscous dominated flow are captured [66]. That allows for the description of a wide range of flow regimes and simulation of a wide range of pore-scale dynamics such as cooperative and/or non-local displacement processes [38]. Such non-local processes have been observed during drainage in 2D micromodels [4,6] and during imbibition [10] in with fast  $\mu$ CT [3,11–13,81]. However, from a computational perspective they are much more expensive than pore network models.

Along with the choice of the size of the computational domain and associated length scale, often implicitly a choice on the underlying flow regime is also made. Avraam and Payatakes [7] demonstrated in 2D micromodels during fractional flow that a ganglion dynamics flow regime exists in combination with connected pathway flow. For ganglion dynamics the non-wetting phase is transported in the form of non-percolating clusters [81]. These move through the pore space in a sequence of breakup and coalescence processes [72], which requires direct numerical simulation to capture [24,31]. Clusters are ultimately mobilized directly or indirectly by viscous forces. Direct mobilization occurs e.g. during “capillary

de-saturation” [57,49,80] where the viscous pressure drop caused by the average wetting phase flow field over non-wetting phase clusters exceeds the capillary trapping forces. For field-relevant flow rates such non-wetting phase clusters can range from a few micrometers [42] to centimeters [5], which easily exceeds the simulation domain size of direct dynamic simulations. Therefore in a respective numerical experiment aiming to determine relative permeability, the contribution of large non-wetting phase clusters to the overall non-wetting phase flux is commonly dismissed.

Mobilization of non-wetting phase clusters can occur in a more subtle way, which has been discovered in a recent study [72]. Cluster dynamics can also occur in capillary-dominated flow, i.e. where the viscous forces associated with the average flow field are not sufficiently large enough to overcome capillary forces and thus cause mobilization. However, the local flow field velocities associated with pore-scale displacement events can exceed the average flow field velocities by orders of magnitude. Haines jumps and snap-off processes are relatively fast events [4] reaching Reynolds numbers near unity [6]. These events range over many pores, indicating that besides capillary and viscous forces also inertial forces become relevant [27] to describe the pore-scale displacement processes. In this way, snap-off processes can trigger coalescence in distant pores connected to the same non-wetting phase cluster [72], which adds to the viscous flow through connected pathways for the non-wetting phase flux. These processes occur on much shorter length scales than the one defining the balance of viscous and capillary forces [5]. The associated processes are typically sufficiently captured by direct dynamic simulators using relatively small computational domain sizes [48,65,66].

Our hypothesis is that if all of the relevant length and time scales associated with the possible flow regimes are captured correctly, then a 1-to-1 match between experiment and simulation would become possible. However, for the computation of relative permeability the question arises of whether there is a significant difference in practice. Large clusters mobilized by viscous forces do contribute to the non-wetting phase flux, no doubt. But if they are infrequent (as percolation models suggest, see [41] and [29]), then their contribution may become negligible. The same holds true for the cluster dynamics caused by non-local and cooperative displacement on smaller length scales. To answer this question, we compared Darcy scale steady-state relative permeability to the relative permeability computed [60] from pore-scale fluid distributions obtained from a synchrotron-based  $\mu$ CT imbibition experiment [13,72]. This approach was already suggested by [40,77], who performed quasi-static drainage  $\mu$ CT experiments, where flow was stopped for imaging, and computed relative permeability from the connected pathway fraction of the resulting fluid distributions using a Stokes flow solver. We advanced this idea in several ways. First, we used pore-scale fluid distributions from a dynamic synchrotron-based  $\mu$ CT imbibition experiment [13,72]. Dynamic means that fluid distributions were imaged under flowing conditions, i.e. the visco-capillary balance was maintained. Second, while in previous studies the approach was used for drainage processes, we performed an imbibition study on sandstone rock. From many pore network modeling studies it is known that imbibition processes are less approachable by quasi-static modeling approaches than drainage processes [58]. While quasi-static approaches consider only the connected pathway contribution, in reality snap-off [71] and other mechanisms cause the non-wetting phase to be at least partially disconnected. Therefore, connected pathway flow and ganglion dynamics may co-exist [72]. For validation of the pore-scale modeling, we then compared steady-state relative permeability measurements conducted on a larger-dimension twin sample from the same block to the pore-scale simulation data from the  $\mu$ CT experiment. Lastly, to assess whether quasi-static modeling is also sufficient

to describe the pore-scale fluid distribution, i.e. for situations where pore-scale fluid distributions are a priori not available, a morphological approach [8,37,75,78] was used to simulate the capillary-dominated invasion process.

## 2. Materials and methods

### 2.1. Porous rock

Gildehauser sandstone [25] was used, which has an average porosity of 20% and a permeability of  $1.5 \pm 0.3$  D. It has low clay content and a narrow pore-size distribution ( $<35 \mu\text{m}$  pore throat diameter), which makes the rock well suitable for  $\mu\text{CT}$  imaging. Also, the relatively high permeability and low capillary entry pressure make the rock suitable for saturation with a low-pressure flow apparatus.

### 2.2. Pore-scale flow experiments and pore-scale imaging

Cylindrical Gildehauser rock samples of 4 mm diameter (which is larger than the representative elementary volume – REV, see Fig. A.1 in Appendix A) and 10 mm length were embedded into a cylindrical polycarbonate flow cell by heat-shrinking. The assembly was mounted on a micro-pump assembly, which includes a micro-piston pump for fluid injection. More details about the setup are described in [10]. N-decane was used as non-wetting phase and brine doped with cesium chloride (10 wt%) as the wetting phase. The interfacial tension between both fluids was  $\sigma = 35 \text{ mN m}^{-1}$ .

The rock sample was first saturated with brine and then n-decane was injected at high rate ( $1000 \mu\text{L/min}$ ) to reach a non-wetting phase saturation around 78%. Then the imbibition experiment was initiated by injecting brine at a volumetric injection rate of  $0.1 \mu\text{L/min}$ , corresponding to a microscopic capillary number of  $Ca_{\text{micro}} = 1.8 \cdot 10^{-8}$  which is defined as  $Ca_{\text{micro}} = \mu_w v / \sigma$  [49]. Here  $\mu_w = 1 \text{ mPa s}$  is the wetting phase viscosity,  $v$  the linear flow velocity of the injected wetting phase. The cluster-based or macroscopic capillary number  $Ca^{\text{macro}} = l^{\text{cl}} / r^p \cdot \varphi \cdot Ca_{\text{micro}}$  [5,13] was between  $9.1 \cdot 10^{-7}$  and  $1.3 \cdot 10^{-6}$  ( $l^{\text{cl}}$  is the length of the non-wetting phase clusters determined from the  $\mu\text{CT}$  images and  $r^p$  is the average pore throat radius), indicating that the flow regime (based on average flow rates) is capillary-dominated. During the flow experiment, 60% of the non-wetting phase (in total  $2.5 \cdot 10^9 \mu\text{m}^3$ ) was mobilized. The flow experiment is described in more detail in [13,72], where saturation as a function of time and the (homogeneous) saturation distribution(s) are also shown.

During imbibition the pore-scale saturation distribution was imaged by synchrotron-based fast X-ray micro-tomography under dynamic flow conditions at the TOMCAT beamline at the Swiss Light Source, Paul Scherrer Institute, Villigen, Switzerland. The beam energy was 37 keV (monochromatic, with a multilayer filter). For flow experiments, 1500 projections were collected at 20 ms

acquisition time using an edge camera (PCO AG, Kelheim, Germany). The spatial resolution was  $2.2 \mu\text{m}/\text{voxel}$  and the temporal resolution for a 3D rendering was 45 s. Scans of the dry samples were obtained at 60 ms acquisition time to obtain a higher-quality image, as displayed in Fig. 1A. It was used for more accurate segmentation of the pore space that is then later used as a mask for segmenting the fluid phases during the flow experiment. The respective greyscale image from the flow experiment is shown in Fig. 1B, where the doped water phase appears in bright and the (undoped) oil in dark. Image processing (filtering and segmentation, see [73] and [74]) was performed with the Avizo Fire 8.0 software package (Visualization Science Group), following a workflow previously described in [10,13,53]. The reconstructed images were first filtered with a non-local means filter and then registered on the dry scan to apply the mask for the pore space of the rock. Then the fluid phases were segmented using a watershed-based segmentation method followed by a cleanup step using morphological operations. An example of the resulting segmented image is displayed in Fig. 1C.

### 2.3. Pore-scale flow simulations

The pore-scale imbibition experiment corresponds in principle to an unsteady-state experiment [58]. However, the accessible length scale of the experiment, i.e. the length of the sample, is smaller than the capillary dispersion zone [72]. Therefore, the Darcy-scale methodology like the analytical JBN inversion technique [46] or history matching with a reservoir simulator [10] cannot be used to determine the relative permeability from the experiment. The pore-scale fluid distribution was available from the  $\mu\text{CT}$  imaging. Single-phase Navier-Stokes flow simulations were performed on the segmented fluid phases obtained from the  $\mu\text{CT}$  imaging during the flow experiment using the software package GeoDict (version 2014; Fraunhofer ITWM, Math2Market GmbH, Kaiserslautern, Germany) directly on the voxel grid from the segmented  $\mu\text{CT}$  images. Wetting and non-wetting phase flow were simulated separately for each time step  $i$  of the experiment (with respective wetting phase saturation ( $S_w^i$ ) using a flow rate of  $10^{-12} \text{ m/s}$  and viscosity of 1 mPa s for the wetting phase and 49.8 mPa s for the non-wetting phase, with a corresponding Reynolds number  $Re \ll 1$ . The resulting permeabilities  $K_w(S_w^i)$  and  $K_o(S_w^i)$  were normalized by the absolute permeability  $K_{abs}$  obtained from a Navier-Stokes flow simulation on the pore space of the dry sample, yielding (in the connected pathway) relative permeabilities as  $k_{r,w}(S_w^i) = K_w(S_w^i) / K_{abs}$  and  $k_{r,o}(S_w^i) = K_o(S_w^i) / K_{abs}$  for the wetting and non-wetting phases, respectively. The obtained relative permeabilities represent the connected pathway flow contribution, but are based on a saturation distribution obtained under dynamic conditions. They do not consider the flux contribution of non-wetting phase ganglion dynamics.

Capillary pressure vs. saturation relationships were approximated with a morphological approach [1,37,75] implemented in

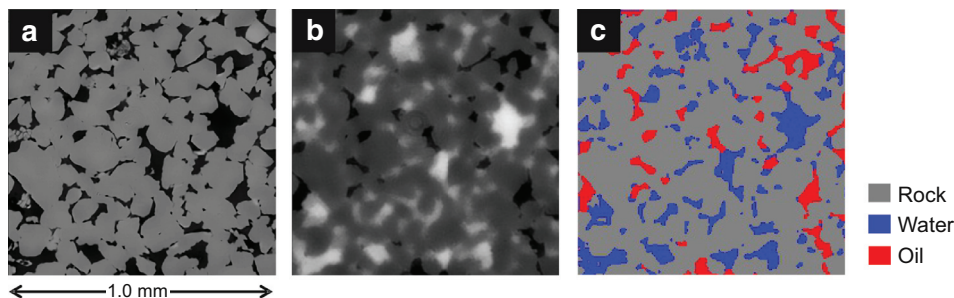


**Fig. 1.**  $\mu\text{CT}$  (greyscale) cross-section of dry Gildehauser rock, (b) greyscale image from the flow experiment, showing the (doped) water (bright) and oil (dark) in the pore space, and (C) segmented image from the flow experiment using the segmented pore space from the dry image to mask the pore space.

GeoDict. Two approximations were applied, which were (i) the morphological approach approximating drainage or imbibition as a sequence of (Young–Laplace) equilibrium states, as opposed to dynamic approaches involving moving liquid–liquid interfaces, and (ii) the Young–Laplace equilibrium states found by a series of morphological erosion and dilation operations using a spherical structuring element. The drainage algorithm starts with a completely water-saturated porous medium and begins with a maximal pore radius  $R$ , which is then decreased step by step. In each step, a pore is drained if (i) the pore radius is larger than  $R$ , (ii) the entering non-wetting phase is connected by pores larger than  $R$  to the non-wetting phase reservoir, and (iii) the replaced wetting phase is connected to the wetting phase reservoir. Conditions (i) and (ii) describe the original algorithm as defined by [37] and used in [8,78]. Condition (iii) introduces a residual wetting phase and was added by [1]. The imbibition algorithm in turn starts with a completely oil-saturated porous medium and minimal pore radius  $R$ , which is then increased step by step. In each step a pore is imbibed if (i) the pore radius is smaller than  $R$ , (ii) the entering wetting phase is connected to the wetting phase reservoir, and (iii) the replaced non-wetting phase is connected to the non-wetting phase reservoir [1]. This approach is computationally less costly than the (capillary-dominated quasi-static) level-set method [44] and also more efficient than simulating the Navier–Stokes equations for two-phase flow with mobile liquid–liquid interfaces. This approach was first used to obtain a simulated mercury–air (Hg–air) intrusion capillary pressure for comparison with experimentally obtained Hg–air intrusion data (often also referred to as mercury intrusion capillary porosimetry, MICP). In a second step the morphological method was also used to simulate drainage and imbibition. From the resulting pore-scale saturation distribution connected pathway flow relative permeabilities were also obtained in a similar way, as described above. In GeoDict this workflow is automated in the SatuDict module. As evident from approximations taken in the workflow the resulting relative permeabilities were entirely quasi-static.

#### 2.4. Steady-state relative permeability measurements

For validation of the pore-scale modeling we compare the pore-scale simulation data from the beamline experiment to steady-state relative permeability measurements conducted on a larger dimension sub-sample from the same block. Darcy-scale relative permeability was determined by a steady-state method [22] using a custom-built X-ray saturation measurement setup at Shell in the Netherlands [9,47]. Cylindrical rock samples of 5 cm height and 3.8 cm (1.5 in.) diameter were first cleaned using Soxhlett extraction with toluene and, subsequently, an azeotrope mixture of chloroform (84%), methanol (14%), and water (2%). After drying, the porosity  $\phi$  was determined by helium porosimetry. The absolute permeability to brine  $K_{abs}$  was determined in a flow experiment from the pressure vs. flux relationship for multiple flow rates according to Eq. (1):

$$q_i = \frac{k_{r,i} \cdot K_{abs}}{\mu_i} \frac{\Delta p_i}{L} \quad (1)$$

Then the sample was mounted inside a sleeve in an X-ray transparent Hassler-type core holder and transferred into the flow setup for steady-state relative permeability measurement by co-injection of saline brine (doped with potassium iodide for increasing the X-ray contrast) and n-decane. The measurements were conducted at constant flow rate, starting with primary drainage where the fractional flow  $f_w$  (which is the ratio of water flux over total flux, see also Eq. (3)) was systematically changed from 100% brine ( $f_w = 1$ ) to 100% oil ( $f_w = 0$ ), followed by 1st imbibition where the fractional flow  $f_w$  was systematically changed from 100% oil ( $f_w = 0$ ) to 100% brine ( $f_w = 1$ ) in 10 saturation steps each. At each saturation step

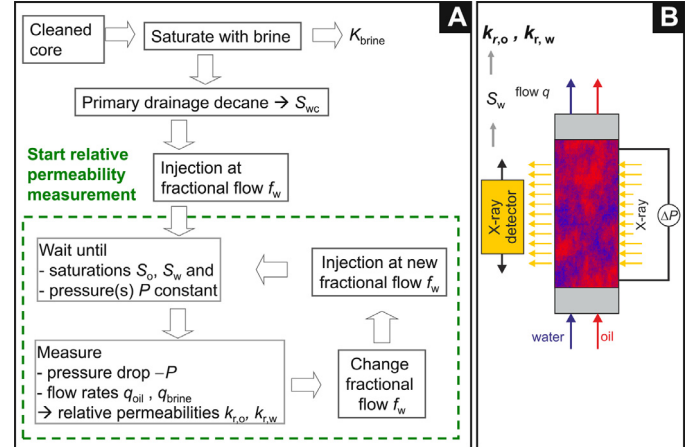


**Fig. 2.** Steady-state relative permeability workflow (A) and schematics of flow setup (B).

$f_w$  was kept constant and the saturation and phase pressures were recorded when steady-state was reached (constant phase pressures and saturations, i.e. in practice variation of the respective averages less than 1% per hour). Pressures were recorded with differential pressure transducers [47]. In addition to flow rates and phase pressures, the saturation profiles at 30 positions along the rock sample were also measured, by X-ray transmission measurements (which are calibrated to both 100% brine and oil saturation). The basic procedure and measurement cycles are sketched in Fig. 2. For details of the equipment, operating procedures and accuracy we refer to [9,47].

From the resulting phase fluxes  $q_i$ , pressure drops  $\Delta p_i$  (using pressure data over length  $L$  of the central part of the sample only) and saturations, the relative permeability could in principle be directly determined using the two-phase extension of Darcy's law (Eq. (1); [22]). However, in order to account for potential capillary end-effects [39], all relative permeability data was obtained by numerical simulation and history matching using Shell's in-house reservoir simulator MoReS ([47,69]). More details on the experimental methodology are given in [9,47].

#### 2.5. Mercury–air intrusion capillary pressure measurements

Mercury porosimetry was used to determine the mercury–air (Hg–air) capillary pressure  $p_c$  [76]. Measurements were performed on smaller sub-samples from the same Gildehauser block using an automatic pore injectivity apparatus (Autopore 9520, Micromeritics). A packing or closure correction is applied during the mercury intrusion, which accounts for packing of mercury around the sample surface prior to entrance of into the pores. The porosity of the sample was determined from the volume of mercury intruded into the sample at 4100 bar, assuming that at this pressure the pore space is completely saturated with mercury.

### 3. Results and discussion

#### 3.1. Relative permeability from μCT flow experiment

The basis for the relative permeability calculation from the μCT flow experiment are the (pore-scale) wetting and non-wetting phase saturation distributions obtained at each time step during the imbibition experiment. The respective connectivity of the wetting and non-wetting phases was determined using the Avizo software package. In our experiment both the wetting and non-wetting phases maintain connectivity between inlet and outlet, i.e. both are percolating. However, as the wetting phase saturation increases, the non-wetting phase becomes increasingly disconnected,

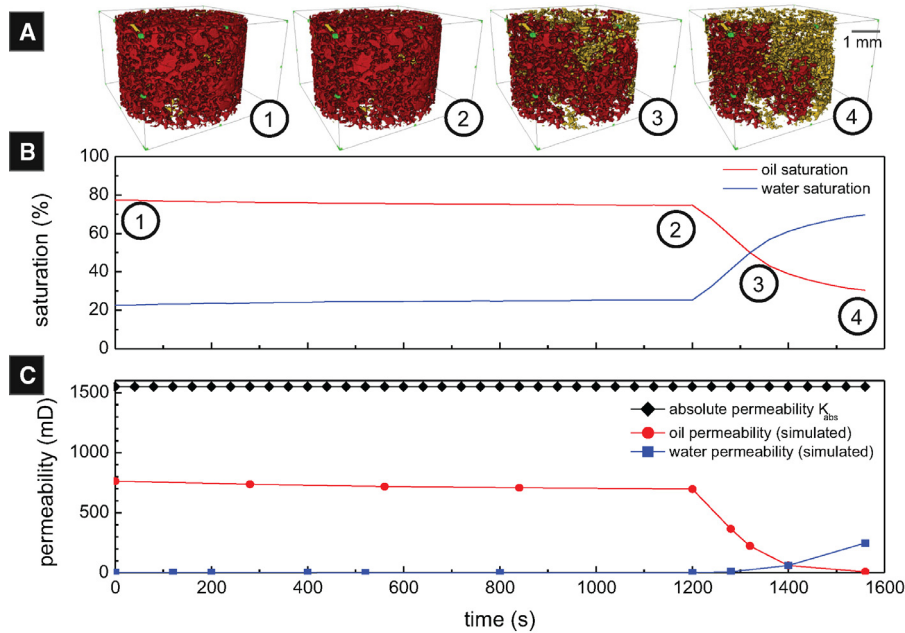


**Fig. 3.** (A) Visualization of the non-wetting phase (oil) distribution from  $\mu$ CT images during the flow experiment indicating the contribution of connected (red) and non-connected (yellow) fraction. (B) Saturation of the wetting phase (water) and non-wetting phase. (C) Absolute permeability  $K_{abs}$ , (connected pathway) for oil and water computed from the pore-scale saturation distribution during the dynamic  $\mu$ CT flow experiment. (For interpretation of the references to color in this figure legend, the reader is referred to the web version of this article).

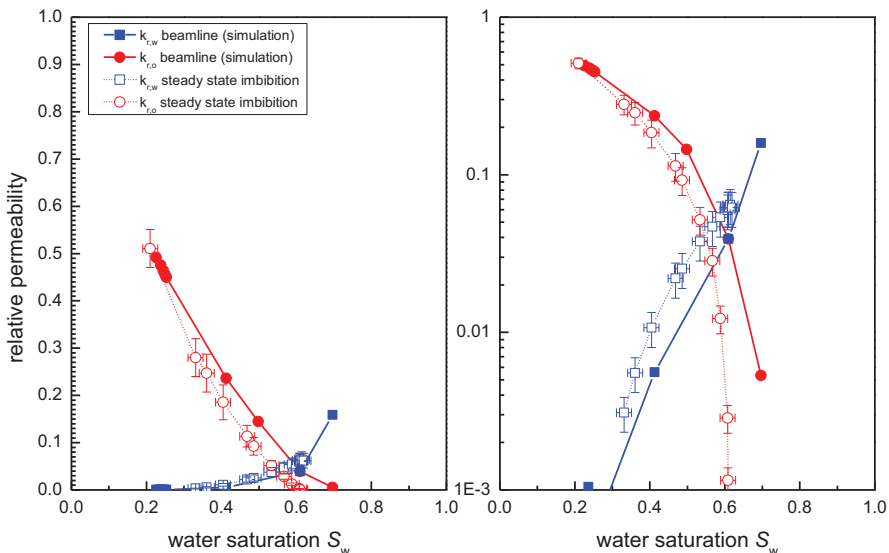


**Fig. 4.** Comparison between experimental steady-state imbibition relative permeability measurements (open dots) and simulations of data derived from the connected phases of the  $\mu$ CT experiment (closed dots) on both a linear (left) and a logarithmic (right) scale as a function of wetting phase saturation  $S_w$ .

which is visualized in Fig. 3A. Initially the non-wetting phase is mostly connected (red). Then during imbibition the fraction of connected non-wetting phase (red) decreases and the fraction of disconnected non-wetting phase increases (yellow). The decrease in non-wetting phase saturation, loss of internal connectivity and its increasing level of fragmentation into disconnected clusters [72] causes the permeability of the oil phase to decrease as shown in Fig. 3C. As the non-wetting phase saturation decreases, in turn the wetting phase saturation increases and consequently the wetting phase permeability increases, as displayed in Fig. 3C. By normalizing the wetting and non-wetting phase connected pathway permeability to the absolute permeability  $K_{abs}$ , the (connected pathway) relative permeabilities were computed and plotted against wetting phase saturation in Fig. 4. Relative permeability-saturation functions often show power law-like behavior [21], with values being

significant (experimental accuracy on flux measurement is about  $10^{-3}$ ) and relevant for practical field applications over three orders of magnitude. Therefore it is customary in the special core analysis community, which in addition to the hydrology community is also addressed in this paper, to always display relative permeability (and also compare different datasets, validate fits etc.) both on linear and logarithmic scales as is done in Fig. 4 and also later figures.

Following the main objective for this study, i.e. to investigate to which extent quasi-static methods are sufficient to estimate relative permeability in imbibition, the results from the quasi-static simulations are validated against a reference dataset from steady-state imbibition experiments. In Fig. 4 the relative permeabilities from the Darcy-scale steady-state imbibition experiments are superimposed for direct comparison. There is fair agreement between

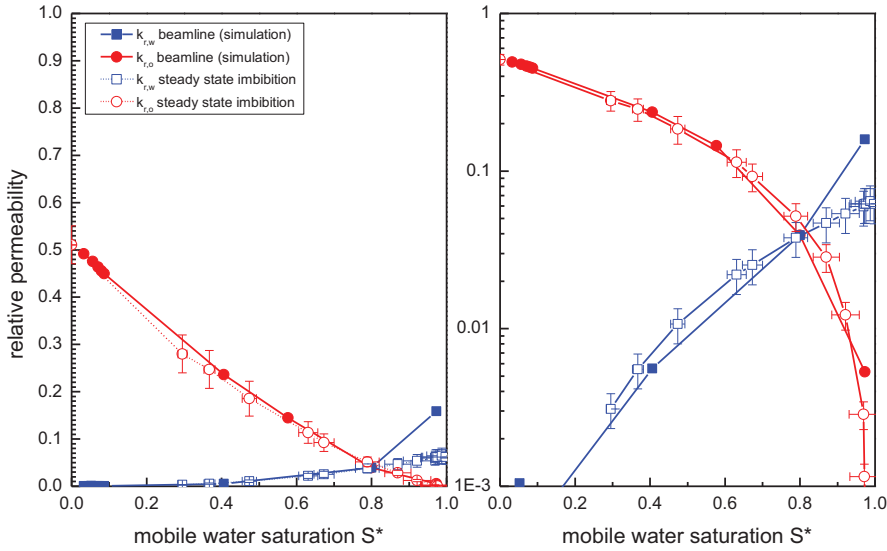


**Fig. 5.** Comparison of experimental steady-state imbibition relative permeability measurement data with simulations from the connected phases of the  $\mu$ CT experiment on both a linear (left) and a logarithmic (right) scale as a function of the mobile wetting phase saturation  $S^*$  (Eq. (2)).

**Table 1**

Corey fit parameters and results of a Buckley–Leverett calculation for the relative data from Fig. 4. Here  $S_{w,c}$  is the connate water saturation,  $S_{o,r}$  the residual oil saturation,  $k_{r,o}(S_{w,c})$  the oil relative permeability endpoint (at connate water saturation),  $k_{r,w}(1-S_{o,r})$  the water relative permeability endpoint (i.e. at residual oil saturation), and  $n_w$  and  $n_o$  are the water and oil Corey exponents, respectively.  $S_w@BT$  is the water saturation at breakthrough,  $f_w@BT$  the respective fractional flow, and Recovery@BT the respective oil recovery.

|                                   | $S_{w,c}$ | $S_{o,r}$ | $k_{r,o}(S_{w,c})$ | $k_{r,w}(1-S_{o,r})$ | $n_w$ | $n_o$ | $S_w@BT$ | $f_w@BT$ | Recovery@BT |
|-----------------------------------|-----------|-----------|--------------------|----------------------|-------|-------|----------|----------|-------------|
| Simulation of $\mu$ CT experiment | 0.21      | 0.29      | 0.56               | 0.16                 | 5.5   | 1.7   | 0.69     | 0.97     | 0.62        |
| Steady-state                      | 0.21      | 0.38      | 0.52               | 0.06                 | 2.4   | 1.6   | 0.62     | 0.99     | 0.52        |

the two datasets in terms of magnitude of relative permeabilities, saturation range, general trends and shape of the curves. The only obvious difference is the saturation endpoint, which for the  $\mu$ CT experiments apparently lies at 10% higher water saturation than for the steady-state experiment.

However, in our experience, such differences in endpoint saturation lie well in the range of sub-sample heterogeneity, and can potentially also be an effect of sample length [5]. To compensate for differences in endpoint saturation, we replotted in Fig. 5 the relative permeability data from Fig. 4 in terms of mobile wetting phase saturation

$$S^* = \frac{S_w - S_{w,c}}{1 - S_{w,c} - S_{o,r}} \quad (2)$$

representing the saturation interval between the irreducible wetting and non-wetting phase (endpoint) saturations,  $S_{w,c}$  and  $S_{o,r}$ , respectively. For the  $\mu$ CT experiment,  $S_{w,c} = 0.21$  and  $S_{o,r} = 0.29$ , and for the steady-state experiment,  $S_{w,c} = 0.21$  and  $S_{o,r} = 0.38$  were used, respectively (see also Table 1).

There is now a better agreement both on the linear and on the logarithmic scale within the experimental error (which for our equipment is approximately 3% for saturation and 10% for relative permeability, see [9]), except for the water endpoint. It is important to mention here that this comparison is very sensitive to the residual oil saturation  $S_{o,r}$  in particular for the dataset obtained from the  $\mu$ CT experiment.  $S_{o,r}$  is very difficult to determine in a reliable way in such dynamic flooding experiments. Centrifuge data would be required for a more reliable determination of  $S_{o,r}$ , but which was not available.

Apart from the difference in endpoint saturation, i.e. after rescaling to the mobile saturation range, there is good agreement between the steady-state measurement and the quasi-static simulation of the beamline experiment. This means that for this particular case, where the non-wetting phase percolates over the

whole saturation range, the contribution of ganglion dynamics (which has been observed in [72]) to the overall non-wetting phase flux is minor.

### 3.2. Impact on fractional flow

The question is now whether the difference between the steady-state experimentally measured relative permeability and the quasi-static simulation from the beamline experiment have any significant implications for practical applications such as oil recovery. Without going into the details of fractional flow, a first good indicator for the amount of recoverable oil is the crossover point between  $k_{r,w}$  and  $k_{r,o}$ . The crossover point indicates the saturation at which the relative permeability of water and oil are approximately the same and it is a first indicator of the approximate economic limit for oil recovery. In Fig. 4 the crossover point for the steady-state data is at  $S_w = 0.54$  whereas for the quasi-static simulation from the beamline experiment the crossover point is at  $S_w = 0.61$ , which is significantly different. Using the normalized mobile saturation data in Fig. 5, the crossover point for both datasets equals at  $S^* = 0.80$  (and the exact endpoint saturation  $S_{o,r}$  can then be determined from a more applicable centrifuge measurement).

For a more detailed analysis, we consider the fractional flow  $f_w$  for the water phase, which is the ratio of the water flux  $q_w$  over the total flux ( $q_w + q_o$ ). In the limit for vanishing capillary pressure ( $p_c = 0$ )  $f_w$  is expressed as [18]:

$$f_w = \frac{q_w}{q_w + q_o} \stackrel{p_c=0}{=} \frac{1}{1 + \frac{k_{r,o}/\mu_o}{k_{r,w}/\mu_w}} \quad (3)$$

where the water viscosity  $\mu_w = 1$  cP, and the oil viscosity is  $\mu_o = 0.92$  cP. In the next step the fractional flow curves  $f_w(S_w)$  were compared between the quasi-static simulation of the  $\mu$ CT experiment and the experimental steady-state data.

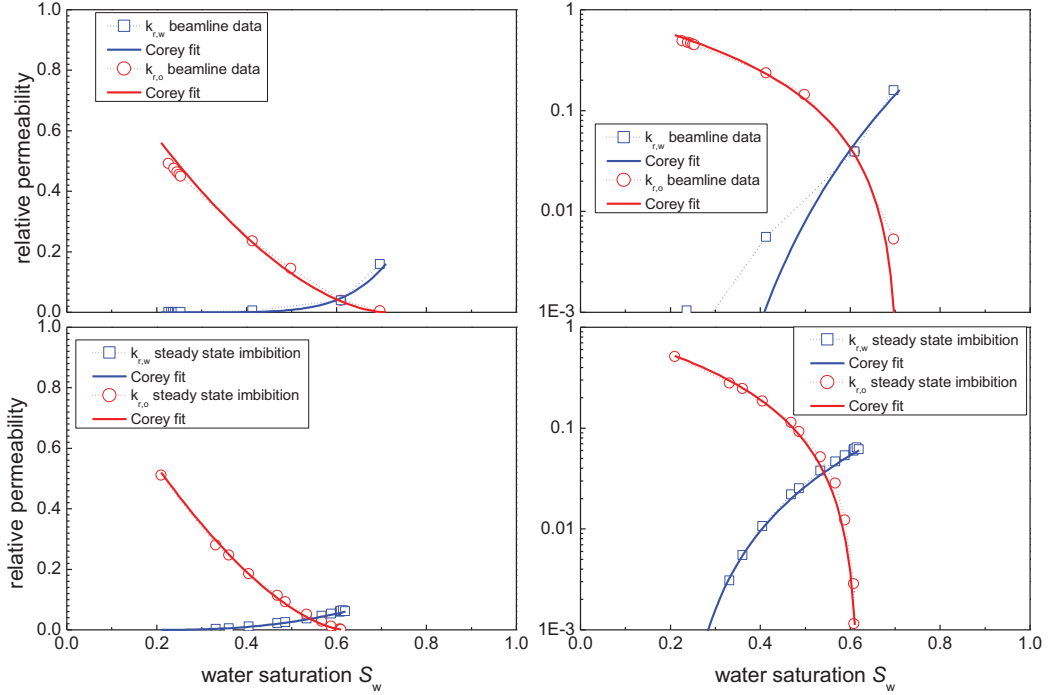


**Fig. 6.** Corey fits of the simulated  $\mu$ CT-based relative permeability (top row) and the steady-state imbibition relative permeability (bottom row) on both a linear (left) and a logarithmic (right) permeability axis.

In addition to  $f_w$  directly computed from the individual data points from Fig. 4, also smoother  $f_w$  curves were computed from fits of the relative permeability data with Corey functions [21,56]:

$$k_{r,w}(S_w) = k_{r,w}|_{S_{w,c}} \cdot (S^*)^{n_w} \quad k_{r,o}(S_w) = k_{r,o}|_{1-S_{o,r}} \cdot (1 - S^*)^{n_o} \quad (4)$$

with the mobile saturation  $S^*$  from Eq. (2). The results of the fit are displayed in Fig. 6, indicating a valid representation of the steady-state data by the Corey function. The respective parameters of the Corey fits, i.e. endpoint saturations and endpoint relative permeability  $k_{r,w}|_{S_{w,c}}$  and  $k_{r,o}|_{1-S_{o,r}}$  and the Corey exponents  $n_w$  and  $n_o$  for water and oil, respectively, are listed in Table 1.

The Corey function parameterizes relative permeability with a smooth curve that follows a power law functionality and the last data point, i.e. the endpoint, should be consistent with the overall trend of the curve representing the other data points. Assuming that relative permeability is well described by Corey functions, the comparison presented in Fig. 6 provides an additional level of consistency and reduces the uncertainty with respect to the endpoint saturation  $S_{o,r}$ . For the simulation data of the  $\mu$ CT experiment, the oil relative permeabilities are represented well by Corey functions but the water relative permeabilities at low saturations clearly deviate from a Corey representation (deviation larger than the experimental error). In particular in the saturation range  $S^* < 0.6$  the agreement for  $k_{r,o}$  is good but for  $S^* > 0.6$  the agreement is modest at best, in particular for the water endpoint. The origin of this particular discrepancy is not clear. However, the impact on the fractional flow curve in Fig. 7 and the breakthrough saturations and recoveries are within the experimental uncertainty.

In Fig. 7, the fractional flow curves of the quasi-static simulation of the  $\mu$ CT experiment were compared with the experimental steady-state data using both the absolute saturation  $S_w$  and the mobile saturation  $S^*$  scales. For 1D displacement in the absence of any capillary pressure, key parameters such as breakthrough water saturation ( $S_w@BT$ ), water cut at breakthrough ( $f_w@BT$ ) and recovery at breakthrough ( $Recovery@BT$ ) of the shock front can be computed analytically from the fractional flow curve  $f_w(S_w)$  using the Buckley–Leverett formalism [18,22]. The graphical repre-

sentation of these calculations is a tangent from  $S_{w,c}$  to the fractional flow curve included in Fig. 7. The saturation at which the tangent intersects with  $f_w$  is the breakthrough saturation, and the respective value of  $f_w$  is the water cut at breakthrough. The results of the Buckley–Leverett calculation for the steady-state experiment and simulation results on basis of the  $\mu$ CT experiment are listed in Table 1. Without normalizing to mobile saturation, there is a difference of 10% in saturation units for recovery at breakthrough between the steady-state experiment and the simulation results, which is roughly the difference in endpoint saturation. On the mobile saturation scale  $S^*$ , the fractional flow curves and the respective tangents are very similar. Consequently, in the hypothetical case that the endpoints were identical, the respective breakthrough saturations and recovery at breakthrough would be identical within less than 5% for both the steady-state experiment and simulation results.

### 3.3. Capillary pressure from the dry pore space using a morphological approach

A comparison between the experimentally measured (MICP experiment) and simulated (using the morphological approach in GeoDict, [8,37,78]) Hg-air capillary pressure  $p_c$  data is displayed in Fig. 8. Note that both cases represent capillary-dominated techniques where the contribution of viscous forces is absent or at least negligible. There is a good agreement between the simulated and the MICP data in a wetting phase saturation range above 0.2, which is similar to observations presented by [40]. The discrepancies at lower wetting phase saturations are related to limitations by the imaging resolution, where the pore space is not fully resolved [53].

### 3.4. Relative permeability from morphological approach

Apart from end-point saturations, relative permeability obtained from quasi-static simulations based on experimentally measured pore-scale fluid distributions show good agreement with steady-state relative permeability reference measurements.

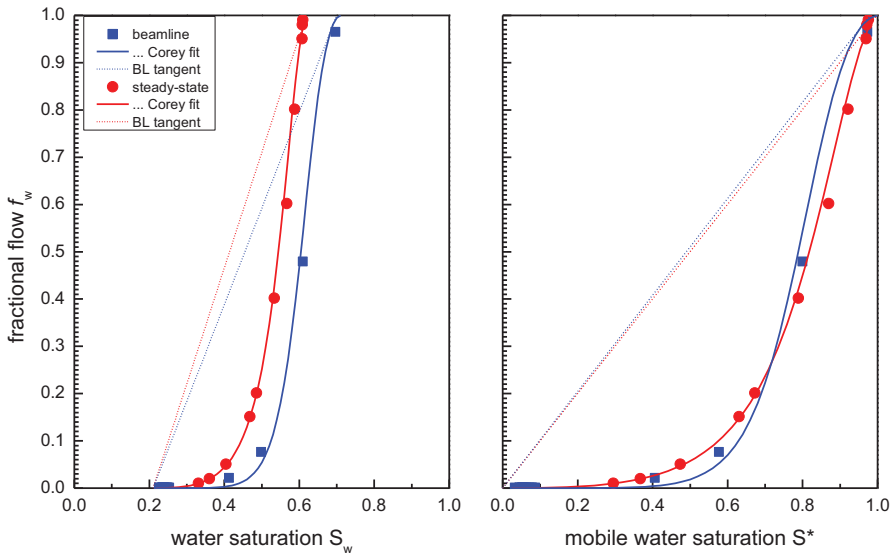


**Fig. 7.** Comparison of the fractional flow curves for the experimental steady-state imbibition relative permeability (measurement) and simulation from the connected phases of the pore scale as a function of the water saturation  $S_w$  (left) and the mobile wetting phase saturation  $S^*$  (right). Here also the position of the shock front is indicated as the point where the tangent meets the fractional flow curve following the Buckley–Leverett (BL) formalism.

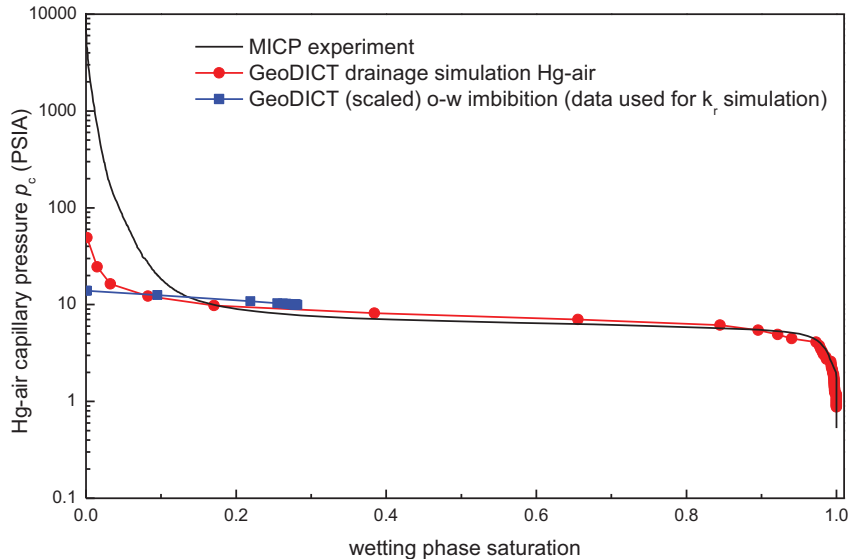


**Fig. 8.** Simulated Hg-air intrusion capillary pressure with morphological approach using GeoDict and comparison with experimental MICP data for Gildehauser sandstone rock. In addition, the GeoDict oil-water “imbibition” capillary pressure simulation scaled to Hg-air by the interfacial tension ratio between oil-water and Hg-air is plotted for comparison.

One may argue that this is good news because for practical applications the computationally much cheaper quasi-static simulation could be used for predicting relative permeability. However, this approach is not practical because the pore-scale fluid distributions of wetting and non-wetting phases are required, which for the presented data requires synchrotron-based  $\mu$ CT flow experiments. Therefore, as the next step a morphological approach [8,37,78] was used to simulate the capillary-dominated invasion process. As already shown in Fig. 8, this approach gives excellent agreement between simulated and measured mercury-air intrusion capillary pressure-saturation relationships. Similar observations have been made for Berea sandstone rock in a previous study [53]. However, mercury-air intrusion is a drainage process. The important question is now how well this approach works for imbibition. Therefore in the next step we simulate pore-scale fluid distributions using the (capillary-controlled) morphological approach [8,37,78] in “imbibition mode” as implemented in GeoDict. Then we compute

the quasi-static hydraulic conductivities on the resulting pore-scale fluid distribution analogous to the approach taken with the  $\mu$ CT data. The final results are compared to the steady-state relative permeability reference data.

The results show that the morphological approach using the “imbibition mode” setting provide relative permeability curves that are more representative of a drainage process than an imbibition process. As displayed in Fig. 9, the resulting imbibition relative permeability shows very large discrepancies from the measured relative permeability and the simulation from the beamline data.

However, the water relative permeability from the morphological approach matches well with the *drainage* steady-state relative permeability as shown in Fig. 10. There are still discrepancies with the oil relative permeability, which indicates that the morphological approach has fundamental difficulties in “simulating” connected oil phases, in particular at low oil saturations.

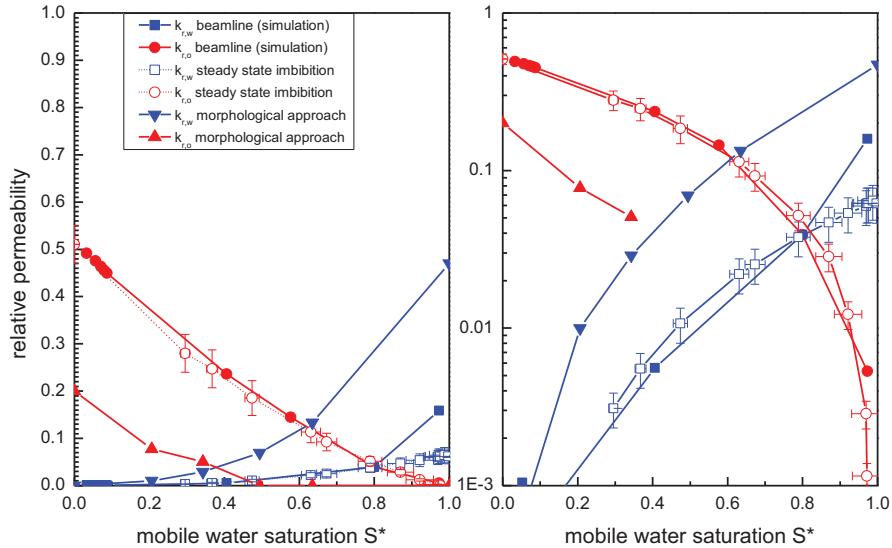


**Fig. 9.** Comparison of experimental steady-state *imbibition* relative permeability (measurement) and simulation from the connected phases of the pore-scale experiment to the morphological approach on a linear (left) and a logarithmic (right) scale as a function of the mobile wetting phase saturation  $S^*$ .

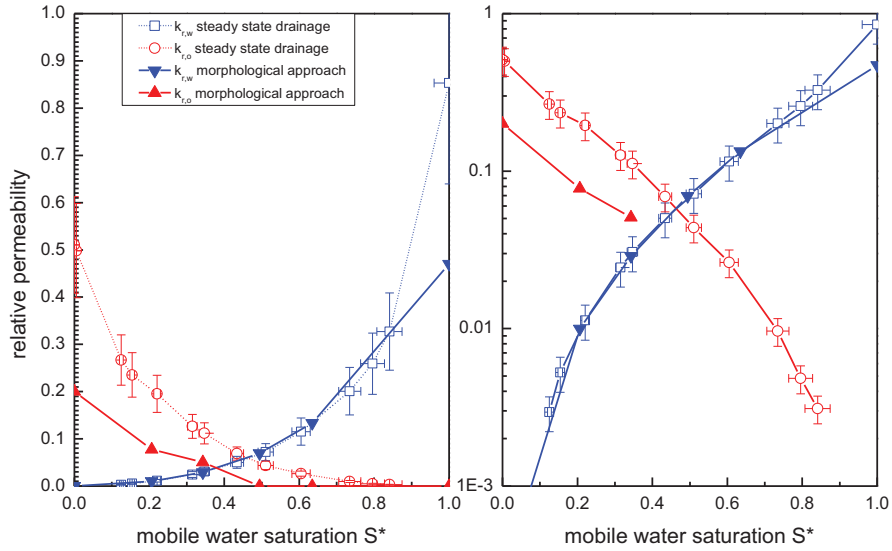


**Fig. 10.** Comparison of experimental steady-state *drainage* relative permeability (measurement) and the morphological approach on a linear (left) and logarithmic scale (right) as a function of the mobile wetting phase saturation  $S^*$ .

Also, the capillary pressure data from Fig. 8, where the scaled oil–water imbibition capillary pressure superimposes with the Hg–air drainage capillary pressure, indicates that the morphological approach approximates more a drainage process with respect to the computed pore-scale fluid distribution. The reason why capillary pressure is predicted reasonably well by the quasi-static method is that the morphological method describes correctly in which pore the non-wetting phase is distributed in individual pores, also probing directly connected pore throats. Also, in a drainage process the conductivity is captured sufficiently well because it is an invasion process where, by design of the algorithm used, both phases are connected.

For imbibition, however, the long-range connectivity of the non-wetting phase is not described very well because processes like snap-off and corner flow are not captured. In reality, there is mass exchange between connected and disconnected fluid phases [33–35], which is not only adding to the net flux but also influences the time evolution of the pore-scale fluid distributions, including the configuration of the connected phases. The morphological approach used here employs local physics to determine the pore-

scale saturation distribution (and hence is conceptually similar to quasi-static pore network modeling which uses local rules). Approaches based on local physics cannot capture the non-local and cooperative processes that have been recently observed in drainage [3,4,6] and imbibition [38,72]. However, our findings show that the local approximation has a more dramatic effect on imbibition than on drainage. Our work clearly shows that this has less to do with the quasi-static computation of the flow field based on a given saturation distribution but rather the approximation of the saturation distribution by a quasi-static morphological approach. A possible explanation can be offered by considering the different pore-scale displacement processes for drainage and imbibition. While for drainage frontal displacement and to some extent cooperative filling are the most relevant process, for imbibition the snap-off and corner flow processes are fundamental to what ultimately determines the connectivity of the non-wetting phase. Snap-off is a process that is influenced by both the local pore and fluid geometry in pore throats, but also the non-local, long-range connectivity of the non-wetting phase which is required to provide the volume of wetting fluid to allow the snap-off to occur [59]. By

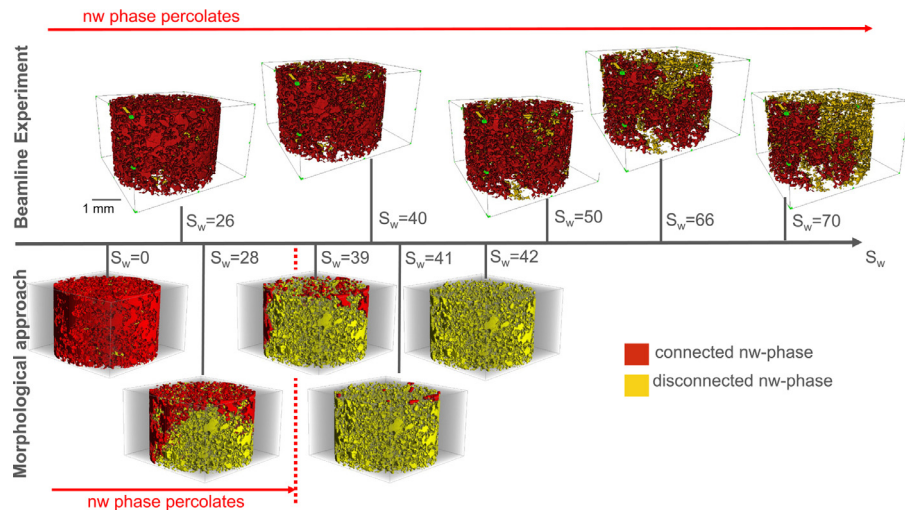


**Fig. 11.** Comparison of the pore-scale fluid distributions from the beamline experiment (top) with the morphological approach from GeoDict in imbibition (bottom) as a function of the wetting phase saturation  $S_w$ . Red indicates a connected and yellow a disconnected non-wetting phase. For the morphological approach the non-wetting phase disconnects i.e. stops percolating at much lower water saturations (around 36–38%) compared to the beamline data where the non-wetting phase percolates up to 70% in this particular experiment. (For interpretation of the references to color in this figure legend, the reader is referred to the web version of this article).

applying only local rules, this long-range connectivity is not considered and only based on local rules snap-off processes are permitted even if the long-range connectivity may suppress them. Also, to capture the physics of corner flow the tiniest crevices of the pore-structure must be imaged and simulated with sufficient resolution. Different realizations of the pore space corners would result in wetting film advancement along different paths and thus ultimately influence the sequence of pore filling events. Therefore the resulting pore-scale fluid distribution is different (and difficult to capture for imbibition), which ultimately leads to a significantly different connectivity and hence relative permeability of particularly the non-wetting phase.

With respect to the data from the morphological approach it is also important to note that the oil relative permeability is only accessible until saturation values of  $S_* \approx 0.4$ . This is because for larger water saturations, i.e. lower oil saturations, the oil phase is not percolating any more, as also illustrated in Fig. 11, and thus the connected pathway hydraulic conductivity is zero. In the morphological approach the saturation value of  $S_w \approx 0.36\text{--}38$  or  $S_* \approx 0.4$  corresponds to a percolation threshold for the non-wetting phase whereas in the experiment the non-wetting phase percolates up to much higher saturations of  $S_w \approx 0.70$ .

Currently, it is not fully clear whether it can be expected in all cases that connected pathway flow will dominate over ganglion dynamics and that the percolation threshold for the non-wetting phase ranges up to  $S_w \approx 0.70$ . Recent studies by Reynolds et al. [70] provide an example with lower percolation threshold and hence more contribution of ganglion dynamics. There the connected pathway flow approach would not succeed to compute relative permeability beyond the percolation threshold.

#### 4. Summary and conclusions

The ability to predict parameters for Darcy-scale flow from quasi-static pore-scale flow simulations conducted directly on the pore space imaged by  $\mu$ CT was investigated. Previous studies have shown reasonably good agreement with Darcy-scale measurements for both drainage and imbibition when using a capillary-viscous flow simulation, which is computationally very expensive [27,48,67,78]. Therefore, the focus here is on quasi-static simulation, which comes at a substantially lower computational cost.

Previous studies [40] have demonstrated that for drainage good agreement with Darcy-scale measurements can be obtained using

a morphological approach to estimate the pore-scale fluid distribution and then conducting quasi-static flow simulations on the connected fluid pathways. We find that for imbibition this approach works well if the pore-scale fluid distributions are available from a flow experiment with  $\mu$ CT pore-scale imaging. Apart from a 10% difference in the endpoint saturation between twin samples, which can also have different origins than the applied methodology, the relative permeability computed on the connected pathway from a synchrotron beamline flow experiment matches closely with the Darcy-scale steady-state measurement. This means that for a given pore-scale fluid distribution where the non-wetting phase percolates over the whole saturation range, the contribution of ganglion dynamics [72] to the overall flux is very minor. However, it is not fully clear whether it can be expected in all cases that connected pathway flow will dominate over ganglion dynamics. Recent studies by Reynolds et al. [70] provide an example that seems to be more dominated by ganglion dynamics and there at least the connected pathway flow approach would not succeed to compute relative permeability, at least not at lower oil saturations.

In summary, we find that quasi-static flow simulations give a good approximation of relative permeability when the pore-scale fluid distributions at each saturation step are known and the oil is mainly connected. If the pore-scale fluid distributions are not available, the approximation with a morphological approach does provide a good basis for the computation of drainage capillary pressure (which matches with measured Hg-air intrusion data very well) but not for imbibition relative permeability. The reason is that quasi-static morphological approaches are not capable of predicting such pore-scale saturation distributions for imbibition. The relative permeability computed from the respective pore-scale fluid distribution using the connected pathway conductivity of the two fluid phases is much closer to a measured drainage relative permeability.

#### Acknowledgments

Ton Blok is gratefully acknowledged for the MICP measurements. Sebastiaan Pieterse and Niels Brussee are gratefully acknowledged for the steady-state relative permeability measurements. Fons Marcelis and Ab Coorn are acknowledged for sample preparation and Soxhlett cleaning. We acknowledge the Paul Scherrer Institut, Villigen, Switzerland for provision of synchrotron

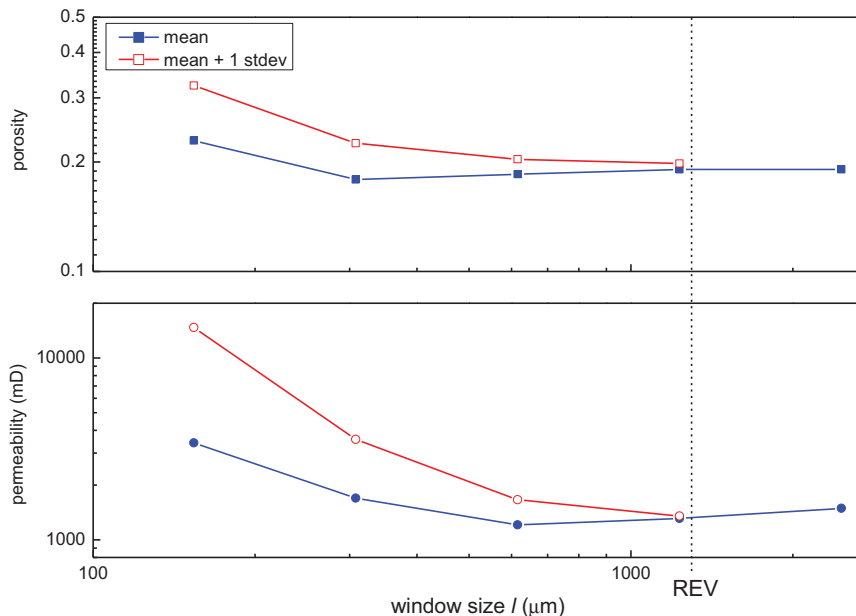


**Figure A.1.** Representative Elementary Volume (REV) analysis with respect to porosity (top panel) and permeability (bottom panel) for Gildehauser sandstone rock following the methodology by ([2]). The REV is estimated from the point where the mean and the mean+1 standard deviation intersection.

radiation beamtime at the TOMCAT beamline of the SLS and would like to thank Sally Irvine and Marco Stampanoni for assistance.

## Appendix A. Representative elementary volume

A representative elementary volume (REV) analysis with respect to porosity and permeability for the Gildehauser sandstone sample used for the synchrotron beamline flow experiments was performed using the  $\mu$ CT image from Fig. 1 following the methodology by [2]. For increasing window size, porosity and permeability values were determined and plotted as a function of window size as shown in Fig. A.1. In addition the mean+1 standard deviation (standard deviation is obtained from multiple sub-samples at same window size) is plotted. According to [2] the intersection between mean and mean+1 standard deviation is an estimate for the REV. The results in Fig. A.1 show that the sample size of 4 mm diameter is larger than the (single phase) REV. Note that while for porosity the mean becomes independent of the window size for windows sizes larger than the REV, for permeability this is not the case because it is not a linear property. Also note that the 2-phase REV can be substantially larger than the single-phase REV [29].

## References

- [1] Ahrenholz B, Tölke J, Lehmann P, Peters A, Kaestner A, Krafczyk M, Durner W. Prediction of capillary hysteresis in a porous material using lattice-Boltzmann methods and comparison to experimental data and a morphological pore network model. *Adv Water Resour* 2008;31:1151–73.
- [2] Al Ibrahim MA, Hurley NF, Zhao W, Acero-Allard D. An automated petrographic image analysis system: capillary pressure curves using confocal microscopy. In: *Proceedings of the SPE annual technical conference and exhibition*, San Antonio, Texas, USA; 2012 8–10 October 2012, SPE.
- [3] Andrew M, Menke H, Blunt MJ, Bijeljic B. The imaging of dynamic multiphase fluid flow using synchrotron-based x-ray microtomography at reservoir conditions. *Transp Porous Media* 2015;110:1–24.
- [4] Armstrong RT, Berg S. Interfacial velocities and capillary pressure gradients during Haines jumps. *Phys Rev E* 2013;88:043010.
- [5] Armstrong RT, Georgiadis H, Ott H, Klemin D, Berg S. Pore-scale mobilization of non-wetting phase ganglia and critical capillary number for onset of macroscopic capillary desaturation. *Geophys Res Lett* 2014;41:1–6.
- [6] Armstrong RT, Evseev N, Koroteev D, Berg S. Velocity field during Haines jumps in porous media. *Adv Water Resour* 2015. <http://dx.doi.org/10.1016/j.advwatres.2015.01.008>.
- [7] Avraam DG, Payatakes AC. Flow regimes and relative permeabilities during steady-state two-phase flow in porous media. *J Fluid Mech* 1995;293:207–36.
- [8] Becker J, Schulz V, Wiegmann A. Numerical determination of two-phase material parameters of a gas diffusion layer using tomography images. *J Fuel Cell Sci Technol* 2008;5(2):021006. <http://dx.doi.org/10.1115/1.2821600>.
- [9] Berg S, Cense AW, Hofman JP, Smits RMM. Two-phase flow in porous media with slip boundary condition. *Transp Porous Media* 2008;74(3):275–92.
- [10] Berg S, Ott H, Klapp SA, Schwing A, Neiteler R, Brussee N, Makurat A, Leu L, Enzmann F, Schwarz J-O, Kersten M, Irvine S, Stampanoni M. Real-time 3D imaging of Haines jumps in porous media flow. *Proc Natl Acad Sci* 2013;10:3755–9.
- [11] Berg S, Oedai S, Ott H. Displacement and mass transfer between saturated and unsaturated CO-brine systems in sandstone. *Int J Greenh Gas Control* 2013;12:478–92.
- [12] Berg S, Armstrong R, Ott H, Georgiadis AH, Klapp SA, Schwing A, Neiteler R, Brussee N, Makurat A, Leu L, Enzmann F, Schwarz J-O, Wolf M, Khan F, Kersten M, Irvine S, Stampanoni M. Multiphase flow in porous rock imaged under dynamic flow conditions with fast x-ray computed microtomography. *Petrophysics* 2014;55(4):304–12.
- [13] Berg S, Rücker M, Armstrong RT, Georgiadis A, Ott H, Leu L, Wolf M, Khan F, Enzmann F, Kersten M. Onset of oil mobilization and non-wetting phase cluster size distribution. *Petrophysics* 2015;56(1):15–22.
- [14] Bijeljic B, Raeini A, Mostaghimi P, Blunt MJ. Predictions of non-Fickian solute transport in different classes of porous media using direct simulation on pore-scale images. *Phys Rev E* 2013;87:013011.
- [15] Blunt MJ, Jackson MD, Piri M, Valvatne PH. Detailed physics, predictive capabilities and macroscopic consequences for pore-network models of multiphase flow. *Adv Water Resour* 2002;25:1069–89.
- [16] Blunt MJ, Bijeljic B, Dong H, Gharbi O, Iglauser S, Mostaghimi P, Paluszny A, Pentland C. Pore-scale imaging and modeling. *Adv Water Resour* 2013;51:197–216.
- [17] Boek ES, Zacharoudiou I, Gray F, Shah SM, Crawshaw JP, Yang J. Multiphase flow and reactive transport at the pore scale using lattice-Boltzmann computer simulations. In: *Proceedings of the SPE annual technical conference and exhibition*, Amsterdam, The Netherlands, 27–29 October 2014; 2014.
- [18] Buckley SE, Leverett MC. Mechanism of fluid displacement in sands. *Trans AIME* 1942;146(1):107–16.
- [19] Chukwodozie C, Tyagi M. Pore scale inertial flow simulations in 3-D smooth and rough sphere packs using lattice Boltzmann method. *AIChE J* 2013;59(12):4858–70.
- [20] Coles ME, Hazlett RD, Spanne P, Soll WE, Muegge EL, Jones KW. Pore level imaging of fluid transport using synchrotron X-ray microtomography. *J Pet Sci Eng* 1998;19:55–63.
- [21] Corey AT. The interrelation between gas and oil relative permeabilities. *Prod Mon* 1954;19(1):38–41.
- [22] Dake LP. Fundamentals of reservoir engineering. Elsevier B.V.; 1978.
- [23] Datta SS, Dupin J-B, Weitz DA. Fluid breakup during simultaneous two-phase flow through a three-dimensional porous medium. *Phys Fluids* 2014;26:062004.
- [24] Demianov A, Dinariev O, Evseev N. Density Functional modelling in multiphase compositional hydrodynamics. *Can J Chem Eng* 2011;89:206–26.
- [25] Dubelaar CW, Nijland TG. Early cretaceous obernkirchen and bentheim sandstones from Germany used as dimension stone in the Netherlands: geology, physical properties, architectural use and comparative weathering. *Geol Soc Lond* 2015;416:SP416–513.

- [26] Dullien FAL. Porous media: fluid transport and pore structure. New York City: Academic Press; 1979.
- [27] Ferrari A, Lunati I. Direct numerical simulations of interface dynamics to link capillary pressure and total surface energy. *Adv Water Resour* 2013;57:19–31.
- [28] Fusseis F, Steeb H, Xiao X, Zhu W-I, Butler IB, Elphick S, Mäder U. A low-cost X-ray-transparent experimental cell for synchrotron-based X-ray microtomography studies under geological reservoir conditions. *J Synchrotron Radiat* 2014;21:251–3.
- [29] Georgiadis A, Berg S, Maitland G, Makurat A, Ott H. Pore-scale micro-CT Imaging: non-wetting phase cluster size distribution during drainage and imbibition. *Phys Rev E* 2013;88.
- [30] Ghanbarzadeh S, Prodanovic M, Hesse M. Percolation and grain boundary wetting in anisotropic texturally equilibrated pore networks. *Phys Rev Lett* 2014;113:048001.
- [31] Gray WG, Dye AL, McClure JE, Pyrak-Nolte LJ, Miller CT. On the dynamics of two-fluid flow in porous media. *Water Resour Res* 2015. <http://dx.doi.org/10.1002/2015WR016921>.
- [32] Hammond PS, Unsal E. A dynamic pore network model for oil displacement by wettability-altering surfactant solution. *Transp Porous Media* 2012;92(3):789–817.
- [33] Hilfer R. Macroscopic equations of motion for two-phase flow in porous media. *Phys Rev E: Stat Nonlinear Soft Matter Phys* 1998;58(2):2090–6.
- [34] Hilfer R. Macroscopic capillarity and hysteresis for flow in porous media. *Phys Rev E: Stat Nonlinear Soft Matter Phys* 2006;73:016307.
- [35] Hilfer R. Macroscopic capillarity without a constitutive capillary pressure function. *Physica A* 2006;371:209–25.
- [36] Hilfer R, Øren PE. Dimensional analysis of pore scale and field scale immiscible displacement. *Transp Porous Media* 1996;22(1):53–72.
- [37] Hilpert M, Miller TC. Pore-morphology-based simulation of drainage in totally wetting porous media. *Adv Water Resour* 2001;24:243–55.
- [38] Holtzman R, Segre E. Wettability stabilizes fluid invasion into porous media via nonlocal, cooperative pore filling. *Phys Rev Lett* 2015;115:164501.
- [39] Huang DD, Honarpour MH. Capillary end effects in coreflood calculations. *J Pet Sci Eng* 1998;19:103–17.
- [40] Hussain F, Pinczewski WV, Cinar Y, Arns JY, Arns CH, Turner ML. Computation of relative permeability from imaged fluid distributions at the pore scale. *Transp Porous Med* 2014;104:91–107.
- [41] Iglauser S, Paluszny a, Pentland C, Blunt MJ. Residual CO<sub>2</sub> imaged with X-ray micro-tomography. *Geophys Res Lett* 2011;38:L21403. <http://dx.doi.org/10.1029/2011GL049680>.
- [42] Iglauser S, Ferno MA, Shearing P, Blunt MJ. Comparison of residual oil cluster size distribution, morphology and saturation in oil-wet and water-wet sandstone. *J Colloid Interface Sci* 2012;375:187–92.
- [43] Jacqmin D. Calculation of two-phase Navier-Stokes flows using phase-field modeling. *J Comput Phys* 1999;155:96–127.
- [44] Jettestuen E, Helland JO, Prodanovic M. A level set method for simulating capillary-controlled displacements at the pore scale with nonzero contact angles. *Water Resour Res* 2013;49:1–17.
- [45] Joekar-Niasar V, Hassanizadeh SM. Uniqueness of specific interfacial area-capillary pressure-saturation relationship under non-equilibrium conditions in two-phase porous media flow. *Transp Porous Media* 2012;94:465–86.
- [46] Johnson EF, Bossler DP, Naumann VO. Calculation of relative permeability from displacement experiments. *Trans AIME* 1959;216:370–2.
- [47] Kokkedee JA, Boom W, Frens AM, Maas JG. Improved special core analysis: scope for a reduced residual oil saturation. In: Proceedings of society of core analysis conference paper, 9601; 1996. p. 1–13.
- [48] Koroteev D, Dinariev O, Evseev N, Klemin D, Nadeev A, Safonov S, Gurpinar O, Berg S, van Kruijsdijk C, Armstrong RT, Myers MT, Hathon L, de Jong H. Direct hydrodynamic simulation of multiphase flow in porous rock. *Petrophysics* 2014;55(4):294–303.
- [49] Lake LW. Enhanced oil recovery. Prentice Hall; 1989.
- [50] Landry CJ, Karpyn ZT, Piri M. Pore-scale analysis of trapped immiscible fluid structures and fluid interfacial areas in oil-wet and water-wet bead packs. *Geofluids* 2011;11:209–27.
- [51] Landry CJ, Karpyn ZT, Ayala O. Pore-scale lattice boltzmann modeling and 4d x-ray computed microtomography imaging of fracture-matrix fluid transfer. *Transp Porous Media* 2014;103:449–68.
- [52] Lenormand R, Touboul E, Zarcone C. Numerical models and experiments on immiscible displacements in porous media. *J Fluid Mech* 1988;189:165–87.
- [53] Leu L, Berg S, Enzmann F, Armstrong RT, Kersten M. Fast X-ray microtomography of multi-phase flow in Berea sandstone: a sensitivity study on image processing. *Transp Porous Media* 2014;105(2):451–69.
- [54] Leverett CM. Capillary behaviour in porous solids. *Trans AIME* 1941;142.
- [55] Manuel D, Van Loo D, Masschaele B, Van den Bulcke J, Van Acker J, Cnudde V, Van Hoorebeke L. Recent micro-CT scanner developments at UGCT. *Nucl Instrum Methods Phys Res* 2014;B 324:35–40.
- [56] Masalmeh SK, Jing XD. capillary pressure characteristics of carbonate, reservoirs: relationship between drainage and imbibition curves, SCA 2006–16. In: Proceedings of the international symposium of the society of core analysts, Trondheim, Norway; 2006 12–16 September.
- [57] Mason G. Mobilization of oil blobs in the pore space of random sphere packings. *Chem Eng Sci* 1983;38(9):1455–60.
- [58] Mason J, Morrow NR. Developments in spontaneous imbibition and possibilities for future work. *J Pet Sci Eng* 2013;110:268–93.
- [59] Mohanty KK, Davis HT, Scriven LE. Physics of oil entrapment in water-wet rock. *SPE Res Eval Eng* 1987;2(1):113–28.
- [60] Mostaghimi P, Blunt MJ, Bijeljic B. Computations of absolute permeability on micro-CT images. *Math Geosci* 2013;45:103–25.
- [61] Niessner J, Berg S, Hassanizadeh SM. Comparison of two-phase Darcy's law with a thermodynamically consistent approach. *Transp Porous Media* 2011;88(1):133–48.
- [62] Porter ML, Schaap MG, Wildenschild D. Lattice-Boltzmann simulations of the capillary pressure-saturation-interfacial area relationship for porous media. *Adv Water Resour* 2009;32(11):1632–40.
- [63] Prodanovic M, Lindquist WB, Serigh RS. Porous structure and fluid partitioning in polyethylene cores from 3D X-ray microtomographic imaging. *J Colloid Interface Sci* 2006;298:282–97.
- [64] Raeesi B, Morrow N, Mason G. Pore network modeling of experimental capillary pressure hysteresis relationships. In: Proceedings of the international symposium of the society of core analysts held in Napa Valley, California, USA; 2013 16–19 September.
- [65] Raeini AQ, Bijeljic B, Blunt MJ. Numerical modelling of sub-pore scale events in two-phase flow through porous rock. *Transp Porous Med* 2014;101:191–213.
- [66] Raeini AQ, Blunt MJ, Bijeljic B. Direct simulations of two-phase flow on micro-CT images of porous media and upscaling of pore-scale forces. *Adv Water Resour* 2014;74:116–26.
- [67] Ramstad T, Øren P-E, Bakke S. Simulation of two phase flow in reservoir rocks using a lattice Boltzmann method, SPE 124617. In: Proceedings of the SPE annual technical conference and exhibition held in New Orleans, Louisiana, USA; 2009 4–7 October.
- [68] Raof A, Nick HM, Hassanizadeh SM, Spiers CJ. PoreFlow: a complex pore-network model for simulation of reactive transport in variably saturated porous media. *Comput Geosci* 2013;61:160–74.
- [69] Regtien JMM, Por GJA, van Stiphout MT, van der Vlugt FF. Interactive reservoir simulation. In: Proceedings of the 13th SPE symposium on reservoir simulation; 1995. p. 545–52. SPE-29146.
- [70] Reynolds C, Menke H, Andrew M, Blunt M, Krevor S. Observations of connected and disconnected non-wetting phase flow during co-injection of N<sub>2</sub> and brine. In: Proceedings of the 7th international conference on porous media & annual meeting held in Padova, Italy; 2015 May 18–21.
- [71] Roof JG. Snap-off of oil droplets in water-wet pores. *SPE J* 1970;10(1):85–90.
- [72] Rücker M, Berg S, Armstrong RT, Georgiadis A, Ott H, Schweng A, Neiteler R, Brussee N, Makurat A, Leu L, Wolf M, Khan F, Enzmann F, Kersten M. From connected pathway flow to ganglion dynamics. *Geophys Res Lett* 2015;42. <http://dx.doi.org/10.1002/2015GL064007>.
- [73] Schlüter S, Weller U, Vogel H-J. Segmentation of X-ray microtomography images of soil using gradient masks. *Comput Geosci* 2010;36:1246–51.
- [74] Schlüter S, Sheppard A, Brown K, Wildenschild D. Image processing of multiphase images obtained via X-ray microtomography: a review. *Water Resour Res* 2014;50:3615–39.
- [75] Silin D, Tomutsa L, Benson S, Patzek TW. Microtomography and pore-scale modeling of two-phase fluid distribution. *Transp Porous Media* 2010;86:495–515.
- [76] Stegemeier GL. Mechanisms of entrapment and mobilization of oil in porous media. Improved oil recovery by surfactant and polymer flooding. Shah DO, RS Schechter, editors. New York: Academic Press; 1977.
- [77] Turner M, Knüfig L, Arns C, Sakellariou A, Senden T, Sheppard A, Sok R, Limaye A, Pinczewski WV, Knackstedt M. Three-dimensional imaging of multiphase flow in porous media. *Physica A* 2004;339:166–72.
- [78] Vogel HJ, Tölke J, Schulz VP, Krafczyk M, Roth K. Comparison of a lattice-Boltzmann model, a full morphology model, and a pore network model for determining capillary pressure-saturation relationships. *Vadose Zone J* 2005;4:380–8.
- [79] Wildenschild D, Sheppard AP. X-ray imaging and analysis techniques for quantifying pore-scale structure and processes in subsurface porous medium systems. *Adv Water Resour* 2013;51:217–46.
- [80] Yadav GD, Mason G. The onset of blob motion in a random sphere packing caused by flow of the surrounding fluid. *Chem Eng Sci* 1983;38(9):1461–5.
- [81] Youssef S, Rosenberg E, Deschamps H, Oughanem R, Maire E, Mokso R. Oil ganglia dynamics in natural porous media during surfactant flooding captured by ultra-fast x-ray microtomograph. In: Proceedings of the international symposium of the society of core analyst, Avignon, France, 11–18 September, 2014; 2014. p. SCA2014–23.